Effect of Rapid Solidification Processing on the Microstructure and Corrosion of 316L Austenitic Stainless Steel

Raíra Chefer Apolinario[a,b]* ![ORCID], Isabela Daianezi[b,c] ![ORCID], Spyridion Haritos Borges[b] ![ORCID],

Lucíola Lucena de Sousa[b] ![ORCID], Haroldo Cavalcanti Pinto[a] ![ORCID], Neide Aparecida Mariano[b] ![ORCID]

[a]Universidade de São Paulo (USP), Faculdade de Engenharia de São Carlos, Departamento de Engenharia de Materiais, João Dagnone Av., 1100 Jd., Sta Angelina, 13563-120, São Carlos, SP, Brasil.
[b]Universidade Federal de Alfenas, Instituto de Ciência e Tecnologia, José Aurélio Vilela Highway, 11999, BR 267, Km 533, 37715-400, Poços de Caldas, MG, Brasil.
[c]Universidade Federal de São Carlos, Departamento de Engenharia de Materiais, Washington Luis Highway, Km 235, 13.565-905, São Carlos, SP, Brasil.

Austenitic stainless steels processed by rolling are widespread in technological applications, since they have excellent mechanical and corrosion properties. This study investigated the effect of the cooling rate, microstructure and properties of 316L austenitic stainless steel under cold rolled conditions and by rapid solidification. The microstructure of the cold rolling processing steel was composed of austenite and a low percentage of delta ferrite. For the rapid solidification condition, the microstructure evolved from columnar and acicular dendrites to equiaxed dendrites with decreasing cooling rates, without the presence of delta ferrite due to the high cooling rate. Furthermore, thermal analyses in both routes revealed that oxidation kinetics was slower after rapid solidification in synthetic air. The microhardness in the cold rolling condition was lower than in the rapid solidification condition since the microstructure under the solidification condition is more refined. The sample in the rapid solidification condition region RS1 presented the highest corrosion resistance considering the pit potential. The passivation current density in the cold rolled condition was $5.72 \times 10^{-5} A/cm^2$, while under the rapid solidification condition, regions RS1 and RS2 were $2.24 \times 10^{-5} A/cm^2$ and $3.72 \times 10^{-6} A/cm^2$, respectively, and region RS3, did not present a passivation region in a broad range of potentials.

Keywords: *Rapid solidification, Cold rolled, Stainless steel, Microstructure.*

1. Introduction

316L austenitic stainless steel is widely used in petrochemicals, mechanical structural components, biomaterials and marine steels due to its excellent corrosion and mechanical resistance properties[1,2]. Nevertheless, its flow resistance is relatively low in the annealed condition, which severely limits its application. Thus, the search for materials with low cost and high specificity has increased the development of grain refinement through new processing routes for stainless steels, such as rapid solidification, melting spinning and laser fusion[3,4].

The study of these innovative technological processes aims at microstructural refinement to improve mechanical behavior and enhance materials processing, and numerous studies analyze the nucleation process, critical growth velocity, growth instability, remelting, and recrystallization of dendrites. The recrystallization process is responsible for grain refinement at high cooling rates[4,5].

Rapid solidification can be performed with cooling rates that can reach 10^6 Ks^{-1} and promote the formation of a refined microstructure, the retention of high-temperature phases, the formation of metastable phases, and the formation of amorphous structures[6-8].

Thus, the microstructure and preferential crystallography orientation of grain growth (texture) and changes in grain morphology generated by rapid solidification are significantly different from conventional manufacturing routes, such as rolling or forging[1,5,7].

It is desirable that changes in alloy composition and cooling rate during rapid solidification affect microstructural growth, as in the dendritic case, and the distribution of the eutectic colonies and intermetallics, in turn, may impact the mechanical properties of the 316 L steel[4-6].

High cooling rates and non-equilibrium microstructures characterize manufacturing by rapid solidification. This generally results in the improvement of mechanical properties. There is also a broad spectrum of microstructures that can be achieved by rapid solidification, varying the cooling rate, and promoting a complete microstructural transition from columnar grains to refined equiaxed grains[6].

Therefore, this work aimed to investigate the microstructure, phase formation, and the resulting mechanical properties of AISI 316 L stainless steel processed by rapid solidification and compare it with the typical as-received condition after cold rolling. Wedge-shaped samples were prepared by suction casting in a copper mold to investigate the influence of various cooling rates on phase formation, microstructure, hardness and corrosion.

*e-mail: raira_scp@hotmail.com

2. Experimental Procedure

The AISI 316L austenitic stainless steel used in this study was cold rolled in the as-received condition with the following dimensions: 50 x 50 mm wide and 5 mm thick, and a chemical analysis was performed by induced plasma atomic emission spectroscopy (ICP-AES). The chemical composition is shown in Table 1.

The cold rolled steel was melted using an arc melting furnace (Compact Arc Melter MAM-1 from Edmund Buehler GmbH) under an atmosphere with an inert gas pressure of 1.0 bar and cooling rate of 10^4 K / s. It was finally cast into the copper mold. The steel obtained after the rapid solidification (RS) process was cut into three regions (1, 2 and 3) in the cross-region from the thinnest to the thickest region, as shown in Figure 1. The samples from regions 1, 2 and 3 were named RS1, RS2 and RS3, respectively, where region (RS1) is located near the liquid metal pouring region, region (RS2) is located in the center of the sample, and region (RS3) corresponds to the final part of the sample.

The microstructures were analyzed by optical (OM) and scanning electron microscopy (SEM), according to the standard ASTM E3-11, and the semiquantitative chemical microanalysis of the phases was performed by energy dispersive spectrometry (EDS) using a windowless silicon drift detector (SDD) for energy dispersive analysis (EDS), after etching in 15ml of HCl + 5ml of HNO_3.

X-ray diffraction (XRD) analyses were performed with Cu Kα radiation. Diffractograms were acquired in a 2θ-range from 10º to 90º, with a step of 0.02º for 2 s/step.

Microstructure analysis by quantitative stereology was performed with the Quantikov Image Analyzer software. Ten image fields were analyzed in each micrograph to calculate phase distribution in each sample.

Vickers microhardness (HV) was measured for the different processing conditions with a load of 0.01 kgf and an indentation time of 15 seconds.

The thermal analysis was performed using differential scanning calorimetry (DSC) and thermogravimetry (TG).

The samples were heated from 25ºC to 1240ºC, at a heating and cooling rate of 10ºC /min, under a synthetic air atmosphere.

Corrosion behavior was evaluated by the cyclic potentiodynamic polarization method using a potentiostat Metrohm model Autolab/PGSTART 302 connected to a typical electrochemical cell with a saturated calomel electrode (SCE) used as a reference electrode. A platinum plate was employed as counter-electrode, and the working electrode was made of the 316L steel after the different manufacturing conditions.

Electrochemical measurements were performed in triplicate for each condition. The electrolyte used was a 3.5 wt.% sodium chloride solution at 25ºC. The potentiodynamic polarization curves were obtained by performing a potential sweep rate of 1mV/s. A sealed glass apparatus was used to place the electrolyte and electrodes, as shown in Figure 2.

3. Results and Discussions

Figure 3 shows the micrographs obtained by optical microscopy and SEM of the steel in the cold rolled condition. Figures 3a and 3b display in the optical micrographs a microstructure formed by equiaxial austenite grains, homogeneously distributed in the matrix, and the presence of deformation twins.

Figures 3c and 3d show the SEM micrographs that confirm the formation of equiaxed grains distributed homogeneously throughout the austenitic matrix (γ), the presence of twins, the presence of deformation caused by cold rolling in the direction ND, and ferrite δ with elongated vermicular morphology, which has also been observed by Araujo et al.[9] and Ahmed et al.[10] for 304 L steel.

Figure 4 shows micrographs obtained by optical microscopy and SEM of the 316L austenitic stainless steel after rapid solidification (RS). The cooling of the rapid solidification was indicated by the arrow on the left, indicating that the cooling rate decreases from RS1 to RS3. Figure 4 (a-c) shows the microstructure in region RS1, composed of columnar dendrites (C.D.) and acicular dendrites (A.D.) of austenite. Figure 4 (d-f)

Table 1. Chemical composition of the 316L austenitic stainless steel (wt%).

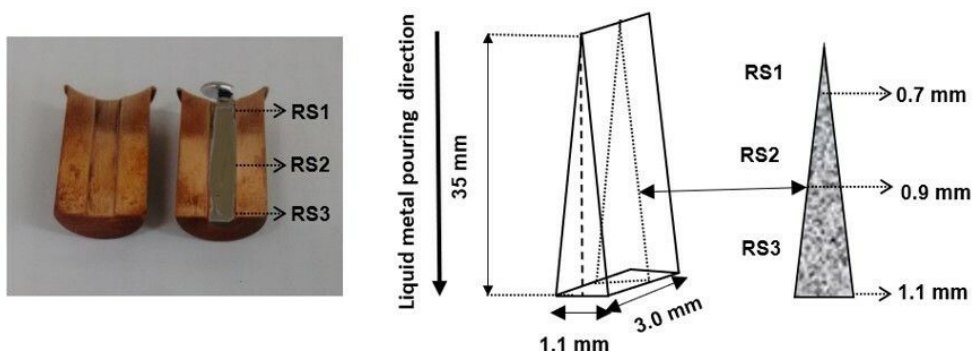| Composition	C	Mn	Si	Cr	Ni	Mo	P	S
316L	0.03	1.39	0.49	16.55	9.97	2.80	0.03	0.01

Figure 1. Alloy melted by rapid solidification in the copper mold, indicating the regions of analysis and schematic representation of the region and dimensions of the samples. The hatched region indicates the normal direction (ND).
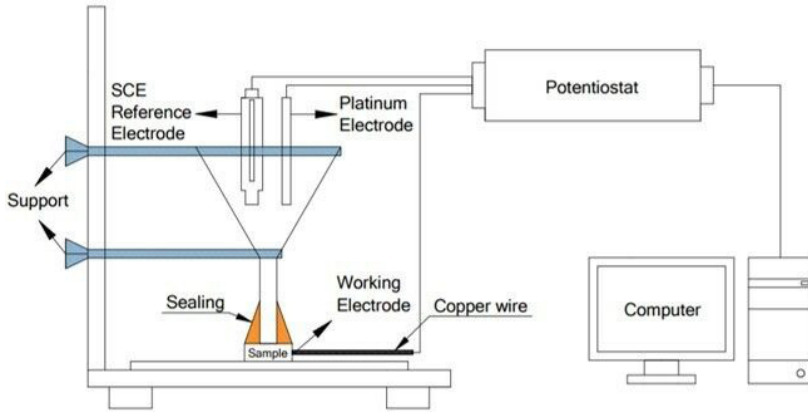
Figure 2. Experimental setup for the electrochemical potentiodynamic measurements.
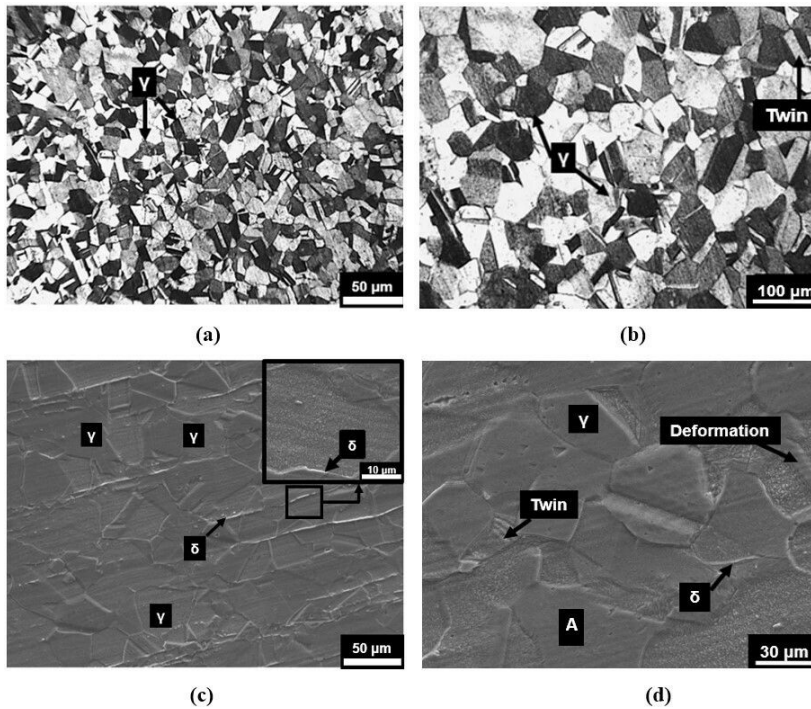

(a)

(b)

(c)

(d)

Figure 3. Micrographs were obtained from the cold rolled 316L stainless steel in direction ND. (a-b) by OM; (c-d) by SEM.

shows the microstructure in region RS2, where the matrix is still austenitic, with the formation of acicular dendrites (A.D.) and equiaxed dendrites (E.D.). Figure 4 (g-i) shows the microstructure in region RS3, where the matrix remains austenitic, but the dendrites are entirely equiaxed (E.D.).

This variation in dendritic morphology among regions RS1, RS2 and RS3 was strictly related to the cooling rate, which depends on sample thickness. The cooling rate can be estimated using the sample thickness R, the initial temperature T_M, and the solidification temperature T_S, adopting the following equation from[11].

$$\dot{T} = dT / dt = K\left(T_M - T_S\right) / CR^2 \qquad (1)$$

where K is thermal conductivity and C is the heat capacity per unit volume. Considering $(T_M-T_S) \sim (2080-1680) \sim 400$ K, K

~ 16.3 W m^{-1} K^{-1} (typical of molten 316L austenitic stainless steel), and C = c*d, where c is specific heat ~ 500 J kg^{-1} K^{-1} and is the weighed density ~ 796 kg m^{-3}, we have:

$$\dot{T} = 0.164 / R^2 \left(K / s\right) \qquad (2)$$

The average cooling rate was estimated as $\sim 10^4$ Ks^{-1} for the wedge regions RS2 and RS3, and $\sim 10^5$ Ks^{-1} for region RS1. Comparing region RS1 with the other regions (RS2 and RS3), a microstructural refinement is observed, since it has a higher cooling rate of $\sim 10^5$ Ks^{-1}.

Quantitative measurements of the volumetric fractions of austenite and δ ferrite, in the conditions as cold rolled and after rapid solidification, were performed using a Quantikov microstructural analyzer software, as shown in Figure 5.

The results corroborate the microstructural analyses of Figure 4, in which δ-ferrite was not formed due to the high solidification temperature and the high cooling rates in the region RS1 of 10^{-5} Ks^{-1} and for the regions RS2 and RS3 of 10^{-4} Ks^{-1}.

The absence of δ ferrite after rapid solidification is desirable due to its magnetic characteristics and because it reduces the mechanical strength and corrosion resistance, according to the literature[12].

Table 2 shows the results of the semiquantitative chemical microanalyses performed by energy dispersive spectroscopy (EDS) of the AISI 316L austenitic stainless steel in the cold rolled and rapid solidification conditions for the regions indicated by A, B, C and D, respectively, in Figures 3d, 4c, 4f and 4i.

The chemical microanalyses were conducted in austenite, in region RS1, where a higher cooling rate occurred owing to the smaller thickness. A slight increase in the Cr, Ni and Mo contents was verified, as well as a decrease in the Fe content due to the solidification temperature. However, in region RS2, despite the lower cooling rate, a chemical composition similar to RS1 was observed.

A Mo enrichment was observed under the conditions of rapid solidification RS1 and RS2. A slight increase in Ni and a reduction in the C content were also observed, compared to the cold rolled condition, similar to the results obtained by Trelewicz et al.[13], using additive laser manufacturing, where it was also observed that inside the grains there is a depletion of C and enrichment of Mo.
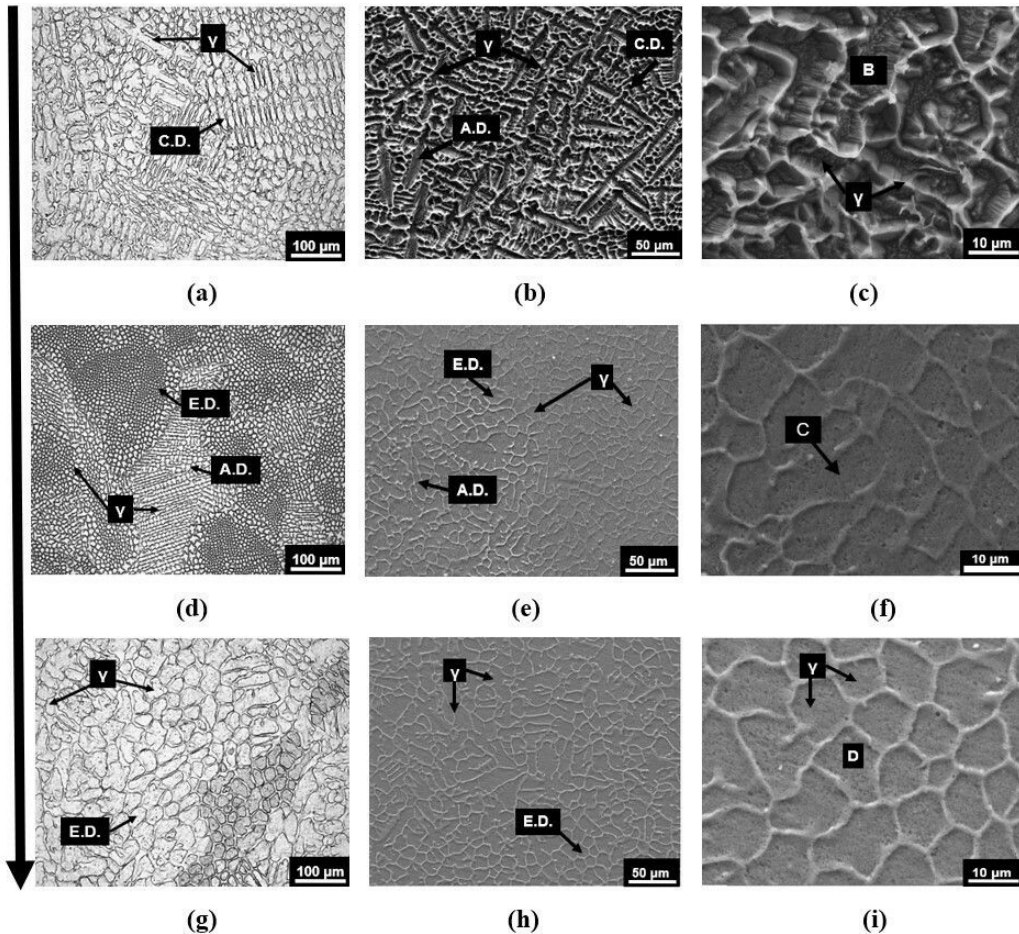

Figure 4. OM and SEM-adjusted micrographs of the 316L stainless steel, rapid solidification processing route. (a-c) Region RS1; (d-f) Region RS2; (g-i) Region RS3. A.D.= Acicular dendritic. C.D.= Columnar dendritic. E.D.= Equiaxial dendritic. γ= austenite phase. B/C/D= region of EDS analysis.

Table 2. Semi-quantitative EDS analyses in the 316L stainless steel after cold rolling and rapid solidification (wt.%).

Processing route	Phase	Fe	C	Cr	Ni	Mo	Si	Mn
Cold rolled	γ (A)	69.66	1.37	16.52	10.36	2.09	-	-
RS1	γ (B)	60.86	-	17.21	14.70	2.89	1.08	-
RS2	γ (C)	64.94	-	17.29	14.40	2.70	0.67	-
RS3	γ (D)	63.36	2.32	16.42	14.53	1.94		1.43

Finally, in region RS3, where the cooling rate was the lowest, the chemical composition was similar to the cold rolled condition, and the presence of Mn was observed to exhibit low solubility temperature, as noted by Maalekian[14], where the solidification temperature of alloying elements for low carbon steels is analyzed.

Nonetheless, for region RS3, inside the grain, as shown in Figure 4i, there is an impoverishment of Mo compared to the cold rolled condition, an increase in C, and a slight reduction in Cr due to a lower cooling rate. The values of the element silicon in the samples of regions RS1 and RS2 are superior to those of the sample under the cold rolled condition, which were obtained by EDS, that is a semiquantitative and localized analysis, which might have led to this variation. Furthermore, the detector used to measure the photon energy in the EDS analysis is of 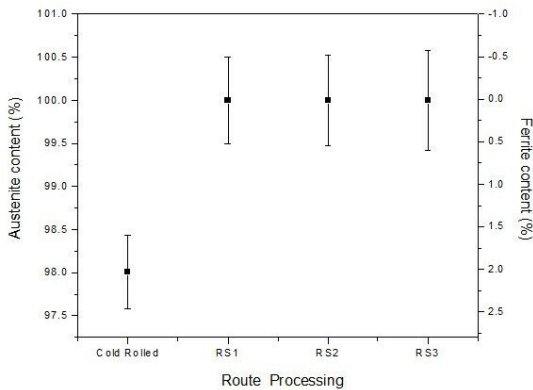silicon, and the silicon ionization of the detector may have occurred and interfered in the semiquantitative analysis of this element[15].

The element Mn was identified in region RS3, but according to David et al.[16], it represents less than 2% (in weight) of the composition. An element mapping was conducted by EDS in region RS3, as displayed in Figure 6a. Region RS3 exhibits a homogeneous microstructure with equiaxial dendrites, as shown in Figure 4 (g-i). The chemical composition is similar to the cold rolled condition, as shown in Figure 6 (b-e). In addition, regions enriched with Fe, Cr, Ni and Mo were observed within the dendritic structure, according to the results shown in Table 2 and the results obtained by[13,17-20].

On the other hand, an impoverishment in C occurs in the interdendritic region, as shown in Figure 6f. The same can be observed for Mo, more concentrated within the dendritic structure.

Figure 7 exhibits the X-ray diffractograms of the 316 L austenitic stainless steel under the cold rolled and rapid solidification conditions (regions RS1, RS2 and RS3). In the cold rolled condition, austenite (face-centered cubic-FCC) and delta ferrite (body-centered cubic-BCC) were observed, thus supporting the micrograph in Figure 3.

The presence of delta ferrite occurs because of cold deformation[9,10,18]. Kurzynowski et al.[21] also observed the presence of a small fraction of delta ferrite in 316 L austenitic stainless steel powder produced by gas atomization, i.e., without cold-work.

The X-ray pattern of Figure 3 was obtained in the normal direction (ND) of the cold rolling and in the regions of rapid solidification (RS1, RS2, RS3). It is possible to observe that region RS2 does not have much texture. Nevertheless, for regions RS1 and RS3, texture is at (200). Additionally, region RS3 has a texture of greater intensity. Also, in the cold rolled condition, Fe-δ is present with strong preferential orientation in (101) and austenite in (200). The peak of delta
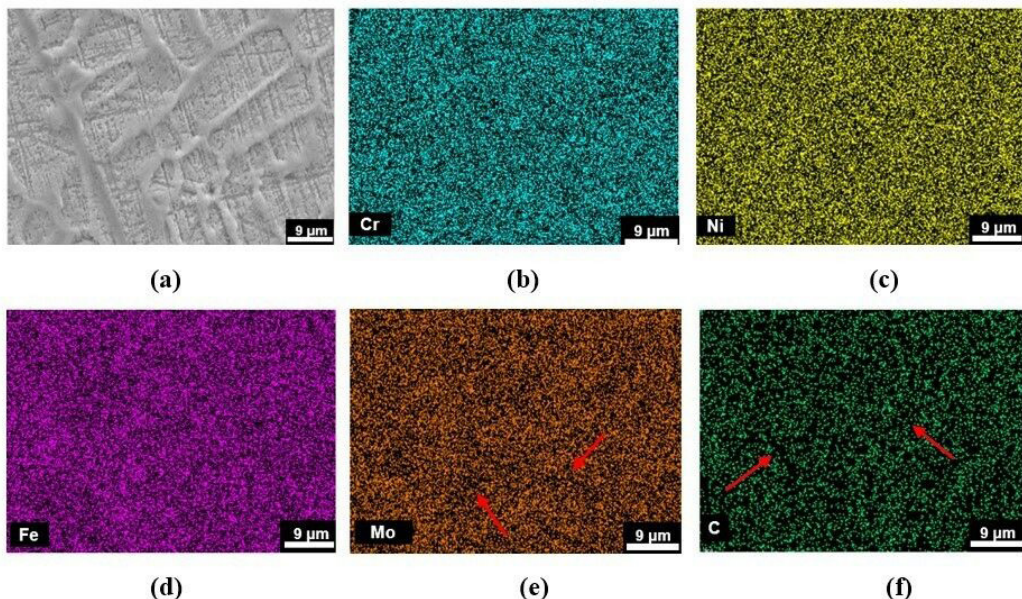

Figure 5. Volumetric fractions of ferrite and austenite in the 316L stainless steel under the following conditions: cold rolled, RS1, RS2 and RS3.

Figure 6. Element mapping by EDS on the 316L stainless steel under the condition of rapid solidification in region RS3. (a) Region RS3; (b) Cr; (c) Ni; (d) Fe; (e) Mo; (f) C.

ferrite presents higher intensity than the peak of austenite, since it presents texture and preferential direction at (101). The texture at (200) of the regions of rapid solidification derives from the growth of columnar grains.

This is in accordance with the Schaeffler diagram, in which the microstructure of the 316 L austenitic stainless steel is composed of austenite with a small percentage between 0 (zero) and 20% of delta ferrite, depending on the ratio of equivalent chromium and nickel, i.e., Cr_{eq} = Cr + Mo + 1.5 Si and Ni_{eq} = Ni + 30C + 0.5 Mn. The higher the Cr_{eq} / Ni_{eq} ratio, the higher the amount of delta ferrite[21,22].

For most combinations of alloy elements present in the 316L steel, the Cr_{eq}/Ni_{eq} ratio varies between 1.4-1.95[22]. Therefore, it results in the solidification with primary ferrite according to the sequence $L \rightarrow (L+\delta) \rightarrow (L+\delta+\gamma) \rightarrow (\gamma+\delta)$[22]. Austenite is a product of the peritectic transformation and Fe-δ undergoes the transformation to austenite during cooling.

Nevertheless, under non-equilibrium conditions, such as rapid solidification processing, and due to the segregation of ferrite stabilizers (Cr, Mo and Si), solidification with primary austenite may occur according to the sequence $L \rightarrow (L+\gamma) \rightarrow (L+\gamma+\delta) \rightarrow (\gamma+\delta)$ [22,23].

Therefore, to interpret the microstructures in Figure 4 and the XRD pattern, the cooling rate was considered. In region RS1, the cooling rate was higher with 10^5 Ks^{-1}. Regarding the data in Table 2, Cr_{eq}/Ni_{eq} corresponds to 1.27, thus causing a solidification path with primary austenite. This can occur according to the solidification sequence $L \rightarrow (L+\gamma) \rightarrow (L+\gamma+\delta) \rightarrow (\gamma+\delta)$. However, the volume fraction of delta (δ) ferrite was very low, as observed in the microstructure in Figure 4 (a-c) and in the XRD pattern in Figure 7.

Furthermore, for the other regions, RS2 and RS3, where the Cr_{eq}/Ni_{eq} ratio corresponds to 1.21 and 1.10, respectively, the solidification sequence $L \rightarrow (L+\gamma) \rightarrow \gamma$ occurs for a cooling rate of 10^4 Ks^{-1}, which is lower compared to region RS1. This corroborates the microstructures in Figures 4(d-f) and 4(g-i) and agrees with the diffractogram in Figure 7, which reveals only austenite. Finally, the condition of the cold rolled sample in the direction ND has a Cr_{eq}/Ni_{eq} ratio of 1.46, which justifies the microstructure of Figure 3 and the XRD pattern.

Figure 8 displays the microhardness (HV) values for the 316L steel in the cold rolled and rapid solidification conditions. It was observed that rapid solidification generates higher microhardness values. This is consistent with several literature data[23,24] in which the microhardness of 316L steel processed by rapid solidification is usually more significant than in the cold rolled condition.

The more elevated microhardness in region RS1 is attributed to the more refined microstructure obtained with a higher cooling rate, as observed in Figure 4c. This results in a high discordance density of austenite, which hinders sliding motion along grain boundaries, thus increasing their strength and resistance to deformation. This high discordance density is impossible to implement in low carbon steels by heat treatment or carbon enrichment. Similar values were achieved, generating a similar microstructure using the laser melting technique for the 316L steel[25-31].

Figure 9 shows the Differential Scanning Calorimetry (DSC) and Thermogravimetry (TG) curves for the 316L steel in the cold rolled and rapid solidification conditions.

In Figure 9a, the DSC heating curve after cold rolling exhibits the occurrence of an endothermic peak at the temperature of 112.3°C, which refers to the loss of adsorbed water, and an exothermic peak at the temperature of 702.7°C, which is attributed to the dissolution of precipitates (carbides and nitrides). At the temperature range between 1075.9°C and 1181.8°C under both conditions, the transformation to a fully austenitic microstructure was observed, thus corroborating the X-ray diffractogram. For the rapid solidification condition, an exothermic peak was observed at the temperature of 677.7°C, attributed to the dissolution of precipitates (carbides and nitrides). The DSC curves of the cold rolled and rapid solidification conditions were similar, with no significant variation. This was also observed by[32] studying the effect of cooling rates on the microstructure of the austenitic 316L stainless steel.

Figure 9b shows the DSC cooling curves. It is observed that after cold rolling, there was an exothermic peak at
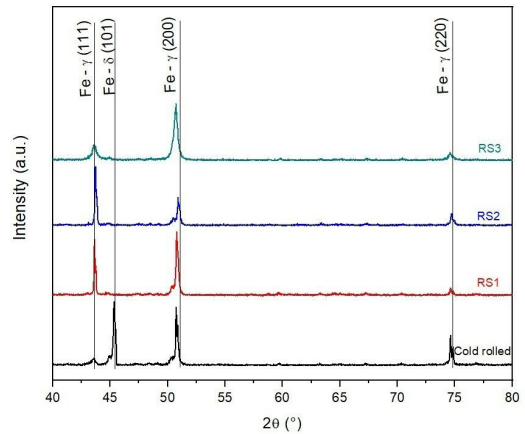

Figure 7. X-ray diffraction spectra of the 316L stainless steel under cold rolling conditions in the direction ND and rapid solidification (regions: RS1, RS2 and RS3).
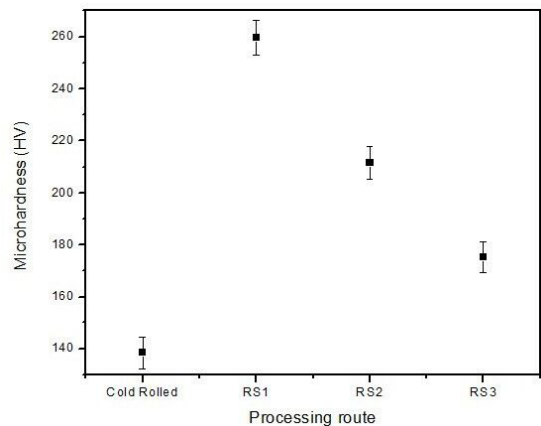

Figure 8. Microhardness (HV) of the 316L stainless steel in the cold rolled and rapid solidification conditions in regions RS1, RS2 and RS3.
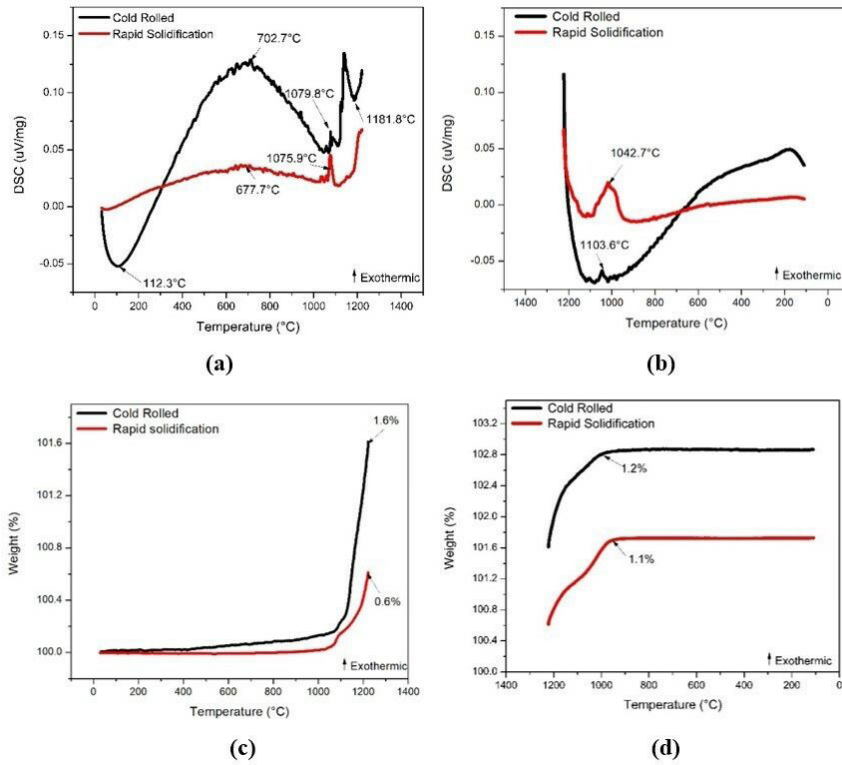
Figure 9. Thermal analysis for austenitic 316L stainless steel in the cold rolled and rapid solidification conditions, using synthetic air as carrier gas. (a) DSC heating curves; (b) DSC cooling curves; (c) TG heating curves; (d) TG cooling curves.

1103.6°C, referring to austenite solidification. In contrast, after rapid solidification, the exothermic peak occurred at a higher temperature, at 1042.7°C. This derives from the fact that after rapid solidification, the Cr, Ni and Mo contents (Table 2) are higher, thus promoting a higher temperature for austenite solidification. Figure 9c shows the thermogravimetry (TG) curves obtained during heating. A mass gain of 1.6% was observed for the cold rolled condition. After rapid solidification, there was a mass gain of 0.6%. Figure 9d shows the thermogravimetry (TG) curves obtained during cooling. A mass gain of 1.2% was verified for the cold rolled condition, whereas 1.1% was observed for the condition of rapid solidification. This mass gain derives from the oxidation reaction suffered by the steel. Additionally, it is observed that the values of mass gain, both during heating and cooling, were lower for the condition of rapid solidification. This can be related to the increased Cr, Ni and Mo contents of austenite, observed by EDS under this condition, that promote higher resistance to oxidation (lower mass gain).

　　Figures 10a and 10b exhibit the open circuit potential (OCP) and cyclic potentiodynamic polarization curves, respectively, in a 3.5 wt% sodium chloride solution at room temperature, from the 316L steel under the cold rolled and rapid solidification conditions. The values of the corrosion potentials (E_{corr}) were extracted from Figure 10a, as specified in Table 3. It was verified that the potentials increased with time, thus characterizing the formation of a passive film on the metallic surface[33-37].

　　From the polarization curves in Figure 10b, the electrochemical parameters were obtained, as shown in

Table 3. Potential for open circuit corrosion of the 316L stainless steel under the cold rolled and rapid solidification conditions in the regions RS1, RS2 and RS3 in a 3.5 wt% sodium chloride solution.

Steel	Route Processing	E_{corr} (mV)
	Cold Rolled	-346 ± 22
316L	RS1	-181 ± 19
	RS2	-180 ± 14
	RS3	-499 ± 18

Table 4. The corrosion potential brought by the open circuit was higher than those obtained by the cyclic potentiodynamic polarization curves, since the partial removal of the passive layer in the polarization scan started at more negative potentials than the corrosion potential.

　　For the conditions cold rolled, rapid solidification regions RS1 and RS2, an anodic current density plateau with a minimum value, which remains with this value over a wide range of potentials was observed from the polarization curves (Figure 10b). This current density establishes the passivity of the steel, identified as passivation current density (Ipass), by the formation of the passive film, with the features of being protective, with good adhesion and good stability, promoting the reduction in corrosion speed. For the condition rapid solidification in the region RS3, it was observed that the polarization curve (Figure 10b) is shifted to higher current densities compared to other conditions.

　　The presence of chlorine ions can cause localized destabilization and rupture of the passive film and initiate localized pit corrosion. Thus, the pit potential (E_{pit}) is defined
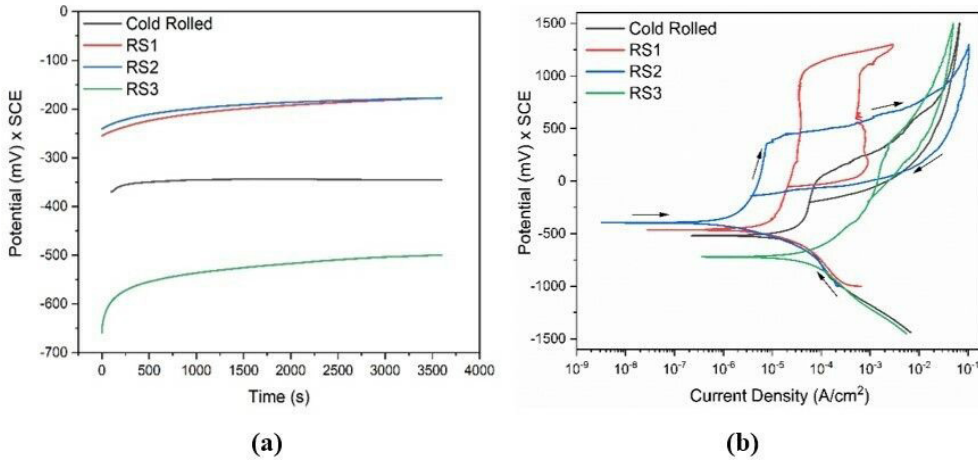
(a)   **(b)**

Figure 10. (a) Open circuit potential; (b) Cyclic potentiodynamic polarization. The arrows indicate the direction of polarization.

Table 4. Electrochemical parameters obtained in a 3.5 wt% sodium chloride solution for the 316L stainless steel under the cold rolled and rapid solidification conditions in regions RS1, RS2 and RS3.

Steel	Route Processing	E_{corr} (mV)	E_{pit} (mV)	I_{pass} (A/cm^2)
	Cold Rolled	-508 ± 14	10 ± 3	$(5.7 \pm 0.4) \times 10^{-5}$
316L	RS1	-455 ± 10	1013 ± 20	$(2.2 \pm 0.3) \times 10^{-5}$
	RS2	-408 ± 24	400 ± 31	$(3.7 \pm 0.4) \times 10^{-6}$
	RS3	-728 ± 22		-

as the potential at which the passive film breaks down and is identified in the potential at which there is a sudden increase in current density, because of pit nucleation, and the more stable the passive film, the higher the Epit value.

The nucleation process and pit growth depend not only on the film property, but also on the oxide/solution interface. The resistance to pit corrosion increases with the rise in Epit, maintaining a passive condition on the surface through a threshold of potential starting from the corrosion potential (E_{corr}). It can be related to the difference between pit and corrosion potentials: $\Delta E_p = E_{pit} - E_{corr}$.

The cold rolled condition presented the smallest passive region ($\Delta E_p = 518$mV), and is related to the break in the passive film at low potentials. The conditions RS1 and RS2 presented superior values, 1468mV and 808mV, respectively.

Region RS1 presented higher pit potential ($E_{pit} = 1013$mV), since the austenite phase in this region has higher Mo and Ni contents, as shown in the semiquantitative analysis presented in Table 2. Region RS1 presented the highest corrosion resistance considering the pit potential. For the condition rapid solidification in the region RS3, did not present a clear passivation region in a broad range of potentials.

The passivation current density (I_{pass}) under the cold rolled condition was 5.72 x 10^{-5} A/cm^2, while under the rapid solidification condition, regions RS1 and RS2 were 2.24 x 10^{-5} A/cm^2 and 3.72 x 10^{-6} A/cm^2, respectively; thus, region SR2 becomes passive before the other conditions.

The corrosion potential was lower for region RS3 ($E_{corr} = -728$mV) because the austenitic phase has lower Cr and Mo contents, as shown in Table 2, favoring the onset of corrosion[33,34].

4. Conclusions

The effect of rapid solidification on the 316 L austenitic stainless steel was compared with cold rolled steel. The microstructure of the cold rolling processing steel was composed of austenite and a low percentage of delta ferrite, which results from cold working, and for the rapid solidification condition, the presence of delta ferrite was not identified due to the high cooling rate. It was also possible to observe the difference in microstructure that evolved from columnar and acicular dendrites to equiaxed dendrites with decreasing cooling rates. Furthermore, the microhardness in the cold rolling condition was lower than in the rapid solidification condition, since the microstructure in the solidification condition is more refined. The cooling rate ranged from 10^{5}K/s^{-1} for region RS1 to 10^{4}K/s^{-1} for regions RS2 and RS3. Furthermore, thermal analyses for 316L steels in both routes revealed that oxidation kinetics are slower after rapid solidification in synthetic air. The sample in the rapid solidification condition region RS1 presented the highest corrosion resistance considering the pit potential. The passivation current density under the cold rolled condition was 5.72 x 10^{-5}A/cm^2, while under the rapid solidification condition, regions RS1 and RS2 were 2.24 x 10^{-5} A/cm^2 and 3.72 x 10^{-6} A/cm^2, respectively, and in the region RS3, did not present a passivation region in a broad range of potentials.

5. Acknowledgments

6. References

1. Sun SH, Hagihara K, Nakano T. Effect of scanning strategy on texture formation in Ni-25 at.%Mo alloys fabricated by selective laser melting. Mater Des. 2018;140:307-16. http://dx.doi.org/10.1016/j.matdes.2017.11.060.

2. Statista. Global stainless steel melt shop production from 2005 to 2020 [Internet]. Hamburg: Statista; 2021 [cited 2021 Sept 29]. Available from: https://www.statista.com/statistics/223028/world-stainless-steel-production/

3. Ishimoto T, Hagihara K, Hisamoto K, Sun SH, Nakano T. Crystallographic texture control of beta-type Ti–15Mo–5Zr–3Al alloy by selective laser melting for the development of novel implants with a biocompatible low Young's modulus. Scr Mater. 2017;132:34-8. http://dx.doi.org/10.1016/j.scriptamat.2016.12.038.

4. Geiger F, Kunze K, Etter T. Tailoring the texture of IN738LC processed by selective laser melting (SLM) by specific scanning strategies. Mater Sci Eng A. 2016;661:240-6. http://dx.doi.org/10.1016/j.msea.2016.03.036.

5. DebRoy T, Wei HL, Zuback JS, Mukherjee T, Elmer JW, Milewski JO, et al. Additive manufacturing of metallic components: process, structure and properties. Prog Mater Sci. 2018;92:112-224. http://dx.doi.org/10.1016/j.pmatsci.2017.10.001.

6. Raghavan N, Dehoff R, Pannala S, Simunovic S, Kirka M, Turner J, et al. Numerical modeling of heat-transfer and the influence of process parameters on tailoring the grain morphology of IN718 in electron beam additive manufacturing. Acta Mater. 2016;112:303-14. http://dx.doi.org/10.1016/j.actamat.2016.03.063.

7. Chinizadeh M, Kiahosseini SR. Deformation, microstructure, hardness, and pitting corrosion of 316 stainless steel after laser forming: a comparison between natural and forced cooling. J Mater Res. 2017;32:3046-54.

8. Xu D, Wan X, Yu J, Xu G, Li G. Effect of cold deformation on microstructures and mechanical properties of austenitic stainless steel. Metals (Basel). 2018;8:522.

9. Araujo APM, Micheloti L, Kiminami CS, Gargarella P. Microstructure, phase formation and properties of rapid solidified Al–Fe–Cr–Ti alloys. Mater. Sci. Technol. 2020;36:1205-14. http://dx.doi.org/10.1080/02670836.2020.1763555.

10. Ahmed II, Da Fonseca JQ, Sherry AH. Effect of strain paths and residual delta ferrite on the failure of cold rolled austenitic stainless steels, type 304L. J Strain Anal Eng Des. 2013;48:410-9. http://dx.doi.org/10.1177/0309324713496086.

11. Inoue H, Koseki T, Ohkita S, Fuji M. Formation mechanism of vermicular and lacy ferrite in austenitic stainless steel weld metals. Sci Technol Weld Join. 2000;5:385-96. http://dx.doi.org/10.1179/136217100101538452.

12. Wang Q, Chen S, Rong L. δ-Ferrite formation and its effect on the mechanical properties of heavy-region AISI 316 stainless steel casting. Metall Mater Trans, A Phys Metall Mater Sci. 2020;51:2998-3008. http://dx.doi.org/10.1007/s11661-020-05717-0.

13. Trelewicz JR, Halada GP, Donaldson OK, Manogharan G. Microstructure and corrosion resistance of laser additively manufactured 316L stainless steel. JOM. 2016;68:850-9. http://dx.doi.org/10.1007/s11837-016-1822-4.

14. Maalekian M. Christian doppler laboratory for early stages of precipitation: the effects of alloying elements on steels – I (Report CDL/ESOP Report Graz). Graz, Austria: Austria Technical Universität Graz, Institut für Werkstoffkunde, Schweißtechnik und Spanlose Formgebungsverfahren; 2007.

15. Dedavid BA, Gomes CI, Machado G. Microscopia eletrônica de varredura: aplicações e preparação de amostras: materiais poliméricos, metálicos e semicondutores. Porto Alegre: EDIPUCRS; 2007.

16. David SA, Vitek JM, Hebble TL. Effect of rapid solidification on stainless steel weld metal microstructures and its implications on the schaeffler diagram. Weld. J. 1987;66. http://dx.doi.org/10.2172/5957599.

17. Dainezi I, Borges SH, Sousa LL, Mariano NA. Temperature and time effect of thermal aging treatment on microstructure and corrosion resistance of UNS S31803 duplex stainless steel. Research Soc Dev. 2021;10(8):e24910817369. http://dx.doi.org/10.33448/rsd-v10i8.17369.

18. Dias D, Nakamatsu S, Della Rovere CA, Otubo J, Mariano NA. Characterization and corrosion resistance behavior of shape memory stainless steel developed by alternate routes. Metals (Basel). 2020;10:13. http://dx.doi.org/10.3390/met10010013.

19. Krakhmalev P, Fredriksson G, Svensson K, Yadroitsev I, Yadroitsava I, Thuvander M, et al. Microstructure, solidification texture, and thermal stability of 316 L stainless steel manufactured by laser powder bed fusion. Metals (Basel). 2018;8(8):643.

20. Pinomaa T, Lindroos M, Walbrühl M, Provatas N, Laukkanen A. The significance of spatial length scales and solute segregation in strengthening rapid solidification microstructures of 316L stainless steel. Acta Mater. 2020;184:1.

21. Kurzynowski T, Gruber K, Stopyra W, Kuźnicka B, Chlebus E. Correlation between process parameters, microstructure and properties of 316 L stainless steel processed by selective laser melting. Mater Sci Eng A. 2018;718:64-73. http://dx.doi.org/10.1016/j.msea.2018.01.103.

22. Ferrandini PL, Rios CT, Dutra AT, Jaime MA, Mei PR, Caram R. Solute segregation and microstructure of directionally solidified austenitic stainless steel. Mater Sci Eng A. 2006;435–436:139-44. http://dx.doi.org/10.1016/j.msea.2006.07.024.

23. Sabooni S, Karimzadeh F, Enayati MH, Ngan AHW, Jabbari H. Gas tungsten arc welding and friction stir welding of ultrafine grained AISI 304L stainless steel: microstructural and mechanical behavior characterization. Mater Charact. 2015;109:138-51. http://dx.doi.org/10.1016/j.matchar.2015.08.009.

24. Bansod AV, Patil AP, Verma J, Shukla S. Microstructure, mechanical and electrochemical evaluation of dissimilar low Ni SS and 304 SS using different filler materials. Mater Res. 2019;22:20170203. http://dx.doi.org/10.1590/1980-5373-MR-2017-0203.

25. Saeidi K, Gao X, Zhong Y, Shen ZJ. Hardened austenite steel with columnar sub-grain structure formed by laser melting. Mater Sci Eng A. 2015;625:221-9. http://dx.doi.org/10.1016/j.msea.2014.12.018.

26. Yusuf SM, Chen Y, Boardman R, Yang S, Gao N. Investigation on porosity and microhardness of 316L stainless steel fabricated by selective laser melting. Metals (Basel). 2017;7:64. http://dx.doi.org/10.3390/met7020064.

27. Suryawanshi J, Prashanth KG, Ramamurty U. Mechanical behavior of selective laser melted 316L stainless steel. Mater Sci Eng A. 2017;696:113-21. http://dx.doi.org/10.1016/j.msea.2017.04.058.

28. Hwa YCS, Kumai TM, Devine N, Yang JK, Yee R, Hardwick K. Burgmann: microstructural banding of directed energy deposition-additively manufactured 316L stainless steel. J Mater Sci Technol. 2021;69:96.

29. Yasa E, Kruth JP. Microstructural investigation of selective laser melting 316L stainless steel parts exposed to laser re-melting. Procedia Eng. 2011;19:389-95. http://dx.doi.org/10.1016/j.proeng.2011.11.130.

30. Anbarasan N, Gupta BK, Prakash S, Muthukumar P, Oyyaravelu R, Kumar RJF, et al. Effect of heat treatment on the microstructure and mechanical properties of inconel 718. Mater. Today Proc. 2018;5:7716-24. http://dx.doi.org/10.1016/J.MATPR.2017.11.448.

31. Corradi M, Di Schino A, Borri A, Rufini R. A review of the use of stainless steel for masonry repair and reinforcement. Constr Build Mater. 2018;181:335-46. http://dx.doi.org/10.1016/J. CONBUILDMAT.2018.06.034.

32. Petrovič DS, Pirnat M, Klančnik G, Mrvar P, Medved J. The effect of cooling rate on the solidification and microstructure evolution in duplex stainless steel: a DSC study. J Therm Anal Calorim. 2012;109(3):1185-91. http://dx.doi.org/10.1007/s10973-012-2370-y.

33. Zhou C, Hu S, Shi Q, Tao H, Song Y, Zheng J, et al. Improvement of corrosion resistance of SS316L manufactured by selective laser melting through subcritical annealing. Corros Sci. 2020;164:108353. http://dx.doi.org/10.1016/j.corsci.2019.108353.

34. Wang S, Ma Q. Characterization of microstructure, mechanical properties and corrosion resistance of dissimilar welded joint between 2205 duplex stainless steel and 16MnR. Mater Des. 2011;32:831-7. http://dx.doi.org/10.1016/j.matdes.2010.07.012.

35. Man C, Duan Z, Cui Z, Dong C, Kong D, Liu T, et al. The effect of sub-grain structure on intergranular corrosion of 316L stainless steel fabricated via selective laser melting. Mater Lett. 2019;243:157-60. http://dx.doi.org/10.1016/j.matlet.2019.02.047.

36. De Carvalho Valeriano L, Otoni Correa E, Mariano NA, Laurent A, Robin M, Tommaselli MAG, et al. Influence of the solution-treatment temperature and short aging times on the electrochemical corrosion behaviour of Uns S32520 super duplex stainless steel. Mater Res. 2019;22(4):20180774.

37. Cappellari De Rezende S, Dainezi I, Apolinario RC, Lucena De Sousa L, Mariano A. Influence of molybdenum on microstructure and pitting corrosion behavior of solution-treated duplex stainless steel in a lithium chloride solution. Mater Res. 2019;22:20190138.